Robust quantum anomalous Hall effect in a pentagonal MoS_2 monolayer grown on CuI(001) substrates

Yimei Fang,[1] Siyu Chen,[2] Xiancong Lu,[1] Shunqing Wu,[1,*] and Zi-Zhong Zhu[1,3,†]

[1]*Department of Physics, OSED, Key Laboratory of Low Dimensional Condensed Matter Physics (Department of Education of Fujian Province) Jiujiang Research institute, Xiamen University, Xiamen 361005, China*

[2]*Cavendish Laboratory, University of Cambridge, J.J. Thomson Avenue, Cambridge CB3 0HE, United Kingdom*

[3]*Fujian Provincial Key Laboratory of Theoretical and Computational Chemistry, Xiamen 361005, China*

(Received 27 September 2020; revised 7 February 2021; accepted 8 March 2021; published 18 March 2021)

Recently, the square planar MoS_2 monolayer, which exhibits the Cairo pentagonal tiling (termed as 1P-MoS_2), was identified as an intrinsic quantum anomalous Hall (QAH) insulator. However, there is a paucity of theoretical work concerning a suitable substrate to support its nontrivial electron transport properties, which is the prerequisite for practical applications. Here. we demonstrate that CuI(001) serves an excellent substrate candidate for epitaxial growth of the 1P-MoS_2 sheet by showing that the intrinsic ferromagnetism and the QAH state of 1P-MoS_2 remain unaltered in the 1P-MoS_2/CuI(001) system. Further analyses of the strain effect on 1P-MoS_2 reveal that the QAH is robust within a strain range from -2% to 2%. Our findings will inspire the experimental realization of QAH effects in two-dimensional (2D) pentagon-based materials.

DOI: 10.1103/PhysRevB.103.115131

I. INTRODUCTION

Two-dimensional (2D) materials epitomized by graphene can exhibit unprecedented physical properties, such as quantum Hall effects. The quantum spin Hall (QSH) effect, first proposed by Kane and Mele for graphene [1] and observed later in HgTe/CdTe quantum wells [2,3], emerges as a topologically nontrivial state of matter. For the QSH state, the time-reversal (TR) symmetry, which protects the helical edge state against geometric disturbances and nonmagnetic impurities [4], is indispensable. By contrast, the realization of quantum anomalous Hall (QAH) effect requires a TR symmetry broken state. A QAH phase is characterized by a finite Chern number [5] and distinguished from trivial insulators by the chiral edge state within the insulating bulk gap [6]. Impregnable to both magnetic and nonmagnetic impurities, the chiral edge state should outperform the helical edge state of the QSH insulator in applications. The relationship between QSH effects and QAH effects appears to be remarkably strong, since the simplest models realizing QSH effects describe electrons with opposite spin carrying opposite quantized Hall conductance [7]. Consequently, the introduction of magnetic impurity into the QSH insulator, such as transition-metal-doped topological insulators [8–10] or decorated topological thin films [11,12], were proposed to support QAH states. Recently, the successful preparation of 2D ferromagnetic insulating materials, such as CrI_3 [13] and $Cr_2Ce_2Te_6$ [14] thin films, enable us to directly explore intrinsic QAH effects in low dimensions.

We note that, so far, numerous 2D ferromagnetic or antiferromagnetic systems have been predicted to host intrinsic QAH states [15–22]. However, most of them adopt hexagonal lattices, which are also popular among other existing monolayer substances. It was only until recently that considerable theoretical and experimental efforts, which were stimulated by penta-graphene [23], were dedicated to search for new 2D substances with Cairo tessellations. Analogous to the isolation of graphene, a pentagonal monolayer would be readily obtained from its van der Waals (vdW) layered counterpart. For example, the pentagonal $PdSe_2$ monolayer [24,25] was successfully isolated from its bulk counterpart by means of micromechanical exfoliation. Interestingly, Liu and Zhuang uncovered the existence of hidden pentagonal layers within bulk compounds enjoying a chemical formula AB_2 and crystallizing into the pyrite structure [26]. They predicted several promising candidates for realizing pentagonal monolayer from a data-mining based analysis. An increasing number of studies have demonstrated that 2D materials with exclusively pentagonal rings can support excellent mechanical and electronic properties, such as a negative Poisson's ratio in penta-graphene [23] and ultrahigh carrier mobility in penta-MX_2 (M = Pd, Pt; X = P, As) [27–29]. Remarkably, Ma *et al.* proposed a family of 2D penta-SnX_2 (X = S, Se, or Te) compounds in which each member is shown to be a large-gap QSH insulator that is feasible for experimental observation under room temperature [30]. More excitingly, intrinsic magnetism, the prerequisite to break TR symmetry, could also be detected in 2D pentagonal sheets. For instance, penta-FeS_2 [31] and penta-CoS_2 [32] were predicted to harbor antiferromagnetic ground states, while the penta-AlN_2 [33] monolayer was reported to be a ferromagnetic insulator. Therefore, it is interesting to explore the possible existence of QAH phases in pentagon based 2D monolayers. A recent paper [34] declared

*wsq@xmu.edu.cn
†zzhu@xmu.edu.cn

 ©2021 American Physical Society

the discovery of the QAH state in a squared pentagonal MoS_2 monolayer. However, the strain and the substrate effects on the QAH state, as well as the stabilities of the pentagonal MoS_2 sheet, were not addressed there.

In this paper, we focus on the experimental feasibility of epitaxially growing 1P-MoS_2 on a substrate and the robustness of the QAH effect on the substrate. The CuI(001) surface which perfectly matches the 1P-MoS_2 monolayer is proved to be a good candidate. From *ab initio* molecular dynamics (AIMD) simulation, we verify the thermodynamic stability of the 1P-MoS_2 monolayer on the CuI(001) substrate. The intrinsic ferromagnetism of the 1P-MoS_2 is found to be preserved in the 1P-MoS_2/CuI(001) system with a slightly enhanced Curie temperature ($T_c = 264$ K) with respect to the freestanding 1P-MoS_2 monolayer ($T_c = 240$ K) owing to the strain effect. Based on the calculations of Chern number and the edge states, we demonstrate that the QAH state of 1P-MoS_2 persists in the 1P-MoS_2/CuI(001) system. Furthermore, we investigate the strain effect on the QAH state of the 1P-MoS_2 monolayer and find that it remains a QAH insulator within the strain range from $-$ 2% to 2%. These results reveal the possibility of realizing QAH effects in 2D pentagon-based materials.

II. COMPUTATIONAL METHODS

First-principles calculations and AIMD simulations were performed based on density functional theory and the projector augment wave [35] method as implemented in the VIENNA AB INITIO SIMULATION PACKAGE (VASP) [36,37]. The exchange-correlation interaction was treated with the generalized gradient approximation (GGA) parameterized by Perdew-Burke-Ernzerhof formula (PBE) [38]. A kinetic energy cutoff of 500 eV was used for wave functions expanded in the plane wave basis. For Brillouin zone integrations, a Monkhorst-Pack [39] k-point mesh of $20 \times 20 \times 1$ was used for the 1P-MoS_2 monolayer. A vacuum layer of $\sim$20 Å was considered to avoid the repeated image interactions. During the structural optimizations, convergence criteria for total energy and atomic forces were set to be 10^{-5} eV and 10^{-3} eV/Å, respectively. Phonon dispersions were performed using the finite displacement approach through PHONOPY code [40]. A 4×4 supercell was constructed to calculate the atomic forces, with an energy convergence criterion of 10^{-8} eV used. The 1P-MoS_2/CuI(001) heterostructure was simulated with three 3×3-CuI(001) trilayers and a 2×2 monolayer of 1P-MoS_2. A k-point mesh of $4 \times 4 \times 1$ and a convergence criterion of atomic forces of 10^{-2} eV/Åwere used in the optimization of the 1P-MoS_2/CuI(001) heterostructure. To account for the vdW interactions, we included the vdW correction to the GGA calculations by using the PBE-D2 method [41]. AIMD simulations were carried out adopting the canonical ensemble with a Nosé-Hoover heat bath [42] for 9 ps with a time step of 3 fs.

III. RESULTS AND DISCUSSION

A. Structures

By comparing the structure of penta-graphene and penta-$PdSe_2$, we notice that two different types of buckling can exist in a 2D material with buckled pentagonal structure. For simplicity, we refer to them as α-type and β-type, respectively. α-type and β-type penta-MoS_2 monolayers, as displayed in Figs. 1(a) and 1(b), respectively, are taken as examples to illustrate the difference between two bucklings. For α-type buckling, coplanar S atoms are bonded together to form S-S dimers, while S atoms in β-type buckling are separated by Mo atoms. By exchanging the z coordinate of the S1 atom with the S2 atom, the α-type bulkling will convert to β-type buckling. Structural relaxation and lattice optimization are performed starting from both types of buckling. However, the results reveal that square instead of pentagonal rings exist in the buckled 1P-MoS_2 monolayers, see Fig. 1(d). Both of the buckled monolayers are nonmagnetic metals.

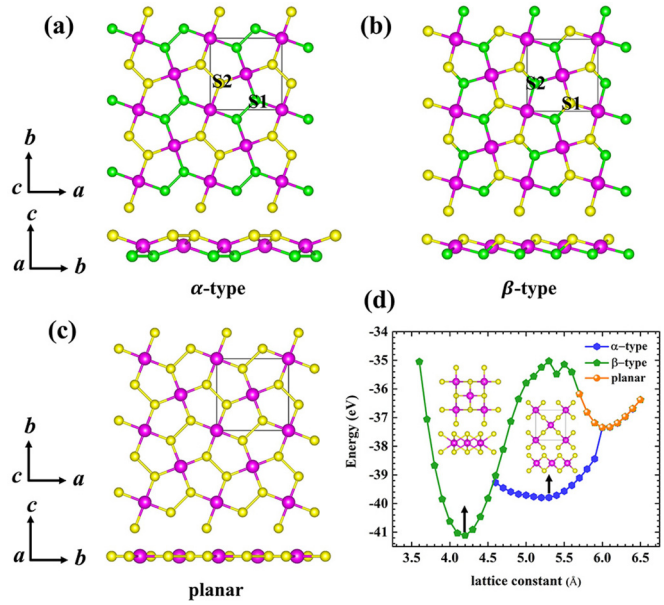

FIG. 1. Top and side views of (a) α-type and (b) β-type penta-MoS_2, where the top and the bottom layers of S atoms are indicated by yellow and green balls, respectively. (c) Optimized planar 1P-MoS_2 monolayer, where the magenta and yellow balls represent Mo and S atoms, respectively. (d) Total energy of penta-MoS_2 monolayers with different types of buckling as a function of lattice constant. The insets show the optimized structures of the penta-MoS_2 monolayers with α- and β-type buckling.

Figure 1(c) depicts the optimized structure of planar 1P-MoS_2. Distinguished from previous reported MoS_2 monolayers, which share a certain thickness originating from the S-Mo-S sandwich structure along z direction, 1P-MoS_2 possesses coplanar Mo and S atoms exhibiting a Cairo pentagonal tiling. This tetragonal lattice belongs to space group P_4/mbm and D_{4h} point group with inversion symmetry preserved. Each primitive cell consists of two Mo atoms and four S atoms with an equilibrium lattice constant of $a = b = 6.04$ Å. Different from 1H-MoS_2, where the sandwiched Mo atoms are six-coordinated to S atoms, Mo atoms in monolayer 1P-MoS_2 are four-coordinated to S atoms. Optimized bond lengths of d_{S-S} and d_{Mo-S} are 2.375 Å and 2.334 Å, respectively.

Although the planar 1P-MoS_2 monolayer was recently proved to host intrinsic ferromagnetism and QAH effect [34], it is energetically less favorable than the buckled ones as

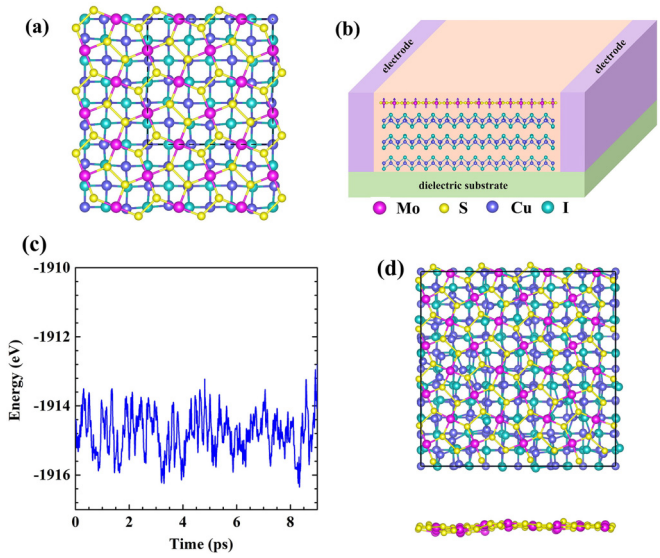

FIG. 2. (a) Optimized crystal structure of 1P-MoS_2/CuI(001) surface from top view. (b) Schematic of the quantum transport device designed from a 1P-MoS_2/CuI(001) heterostructure, where the purple arrows denote spin directions. (c) Fluctuation of total energy of the 1P-MoS_2/CuI(001) system during the AIMD simulation. (d) Structure snapshots of the 1P-MoS_2/CuI(001) system at the end of the simulation.

indicated in Fig. 1(d). Given that 1P-MoS_2 has larger lattice constants than that of buckled ones, an appropriate substrate that provides the required tensile strains to beat the buckled rivals is indispensable in order to stabilize the 1P-MoS_2 monolayer and support its nontrivial electronic structures. Before we discuss the stability of the 1P-MoS_2 monolayer on the CuI(001) substrate, the dynamical, thermodynamical, and mechanical stabilities of pristine 1P-MoS_2 are verified (see supplementary notes, Fig. S1, and Table S1 in the Supplemental Material [43]).

B. Stability of 1P-MoS_2 on CuI(001) substrate

Generally, an ideal substrate should behave as an insulator, and should not strongly interact with the 2D sample or impose large strain on it. We notice that bulk CuI which crystallizes in $P4/nmm$ symmetry with quasi-2D layered structure should serve as an ideal candidate, since it harbors a large band gap of 1.52 eV and the in-plane lattice mismatch between a 3×3 CuI(001) surface and a 2×2 1P-MoS_2 monolayer is only 1.5%. The perfect lattice match between the CuI(001) surface and the 1P-MoS_2 monolayer will only induce tiny strains on 1P-MoS_2, assuring that the interlayer interaction is sufficiently strong to break the symmetry. Figure 2(a) depicts the optimized structure of the 1P-MoS_2/CuI(001) surface, where all Mo atoms in the supercell overlay the Cu-I bridge sites. The vertical distance between the topmost layer I atoms and the 1P-MoS_2 monolayer is 3.37 Å. The binding energy of the heterostructure is estimated to be −35.8 meV/atom, indicating a typical vdW interaction in the 1P-MoS_2/CuI(001) heterostructure.

We further examine the thermodynamical stability of the 1P-MoS_2/CuI(001) system by performing AIMD simulation. A large supercell containing three 6×6-CuI(001) trilayers and a 4×4 monolayer of 1P-MoS_2 is constructed to perform the simulation. As shown in Fig. 2(d), the pentagonal building blocks of the 1P-MoS_2 sheet are well preserved despite being corrugated after heating at 300 K for 9 ps, suggesting that the 1P-MoS_2/CuI(001) system is thermodynamically stable at room temperature.

C. Magnetism

Given the fact that there is no charge transfer between the 1P-MoS_2 overlayer and the CuI(001) substrate, we construct a stretched 1P-MoS_2 monolayer model under 1.5% tensile strain to study the magnetic behavior of the 1P-MoS_2 overlayer. To identify the ground-state magnetic ordering of 1P-MoS_2 with 1.5% strain, we perform both spin-unpolarized and spin-polarized calculations considering nonmagnetic (NM), ferromagnetic (FM) and Néel-type antiferromagnetic (AFM) configurations to acquire their self-consistent total energies. The results indicate that for 1P-MoS_2 the FM state is energetically preferable to AFM and NM states by 42.3 meV/atom and 157.5 meV/atom, respectively. The calculated spin moment per Mo atom is ∼1.89 μ_B, indicating that each Mo atom has two unpaired electrons. This is consistent with the $Mo^{4+}(d^{2\uparrow}_{xz,yz})$ ionic configuration from the crystal filed splitting analysis. Under the square planar coordination, the $4d$ orbitals of Mo atoms split into three nondegenerate states (i.e., $d_{x^2-y^2}$, d_{xy}, and d_{z^2}) and a doubly degenerate $d_{xz,yz}$ state, resembling the splitting of Ir $5d$ orbitlas in Na_4IrO_4 [48]. The crystal filed splitting is weak here and thus all the nondegenerate states are empty, while the doubly degenerate $d_{xz,yz}$ state is half-filled with parallel spins, leading the Mo ions to be in the $Mo^{4+}(d^{2\uparrow}_{xz,yz})$ configuration. Interestingly, the induced spin magnetic moments on the S atoms are significant (∼0.11 μ_B/S) and antiparallel to those of Mo atoms. This phenomenon suggests that the long-range ferromagnetism in 1P-MoS_2 is resulted from a FM superexchange between the partially filled d orbitals of Mo atoms and p orbitals of the intervening S atoms.

Magnetic anisotropy energy (E_{ma}), which refers to the energy barrier between the hard-axis and easy-axis magnetizations, constitutes an important parameter to characterize a FM material. Here, E_{ma} is determined as $E_{ma} = E_{100} - E_{001}$, where E_{100} and E_{001} denote the total energies of in-plane and out-of-plane magnetizations, respectively. The calculated positive value of E_{ma}= 3.55 meV/(f.u.) indicates that 1P-MoS_2 prefers an out-of-plane easy axis, which contributes to eliminate the Mermin-Wagner restriction in 2D materials [13,49]. Consequently, the long-range ferromagnetic order would be possible to persist in the 1P-MoS_2 monolayer at finite temperatures.

For further exploration of exchange interactions in 1P-MoS_2, we calculate the nearest-neighbor exchange coupling parameter J_1 by mapping the total energies of FM and AFM configurations onto the effective Heisenberg Hamiltonian,

$$E = E_0 - \sum_{i,j} J_{i,j} \hat{\mathbf{e}}_i \cdot \hat{\mathbf{e}}_j \quad (1)$$

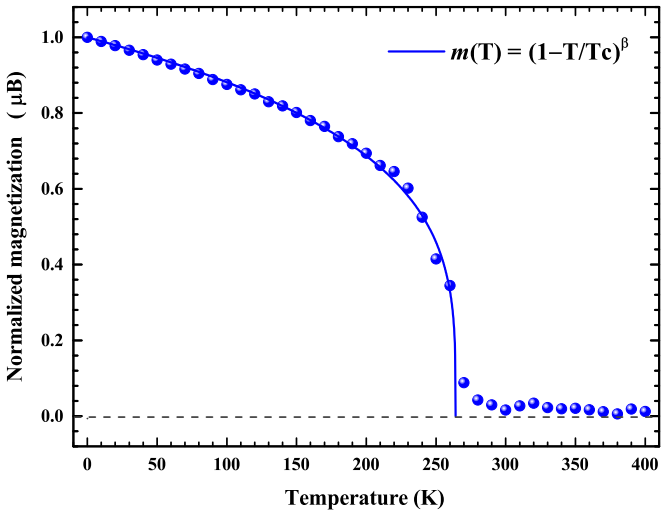

FIG. 3. Temperature-dependent normalized magnetization for the 1P-MoS_2 monolayer under 1.5% strain obtained from the Monte Carlo simulation. Blue dots indicate the simulated mean magnetization, and the blue solid line represents the corresponding fit based on Eq. (2).

where E_0 donates the NM ground-state energy, J_{ij} is the exchange integral between the i-th and j-th Mo atoms, and $\hat{\mathbf{e}}_i$ ($\hat{\mathbf{e}}_j$) is the unit vector indicating the direction of magnetic moment on sites i (j). J_1 can be further expressed as $J_1 = (E_{\mathrm{AFM}} - E_{\mathrm{FM}})/8$. The estimated large positive J_1 value of 31.7 meV reveals strong FM coupling between nearest-neighbor Mo atoms. By employing the VAMPIRE package [51], the Curie temperature (T_c) of the stretched 1P-MoS_2 under 1.5% strain can be determined via Monte Carlo simulation based on the calculated J_1 and E_{ma}.

The simulated system for the stretched 1P-MoS_2 under 1.5% strain consists of a nanosheet of 60 nm × 60 nm in size, which is sufficiently large to reduce the finite-size effects. Figure 3 depicts the resultant temperature-dependent normalized magnetization using 20000 equilibration steps and 30000 averaging steps. Fitting the simulated results (blue dots) to the equation,

$$m(T) = \left(1 - \frac{T}{T_c}\right)^{\beta}, \tag{2}$$

yields a critical exponent β of 0.26 and an estimated T_c of 264 K, which is approaching the room temperature and higher than that of CrI_3 [13] and $Cr_2Ge_2Te_6$ [14]. For comparison, a similar simulation of the T_c for pristine 1P-MoS_2 is shown in Fig. S2 [43]. Our result reveals that the T_c value of 1.5%-strained 1P-MoS_2 is slightly larger than that of pristine 1P-MoS_2 by 24 K, owing to the enhanced exchange energy under tensile strains.

D. Electronic structures and QAH state

In what follows, we investigate the electronic structures of the 1P-MoS_2/CuI(001) heterostructure. For comparison, the spin-polarized band structures of the pristine 1P-MoS_2 monolayer and the 1P-MoS_2/CuI(001) heterostructure are shown in Fig. S3 and Fig. S4 [43], respectively. As shown in Fig. S4,

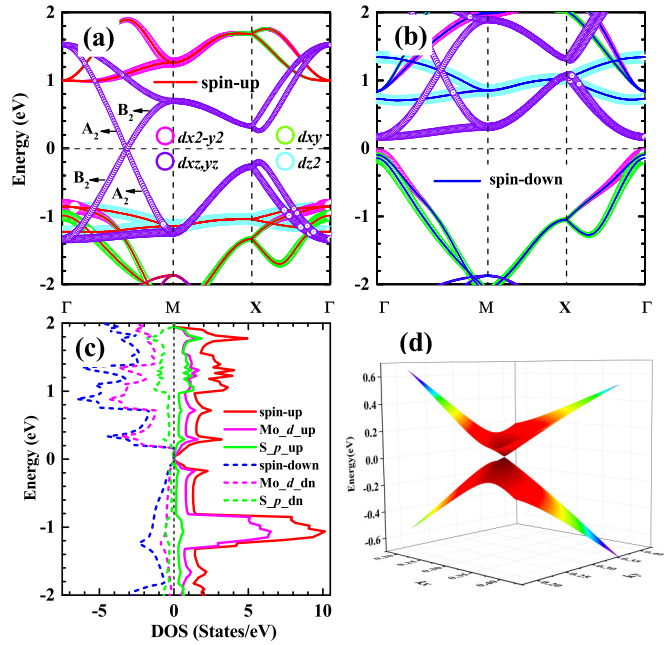

FIG. 4. Spin-polarized band structures without SOC for (a) spin-up and (b) spin-down channels for the 1P-MoS2 monolayer under 1.5% tensile strain. The symmetries of the band states along the Γ-M path are labeled according to the irreducible representation of the C_{2v} point group with the aid of the QUANTUM ESPRESSO package [50]. (c) Spin- and site-projected DOS. (d) 3D band structure for spin-up channel enlarged at the band crossing point (0.29, 0.29)$2\pi/a$.

the Dirac cone is retained intact in the spin-up channel in the 1P-MoS_2/CuI(001) system while the spin-down channel still exhibits semiconducting behavior when SOC is ignored. For simplicity, we show the spin-resolved band structures as well as the spin- and orbital-projected density of states (DOS) in Fig. 4 for the 1P-MoS_2 monolayer with 1.5% strain to explore the underlying reasons for the emergence of the exotic Dirac half-metallic state in 1P-MoS_2. From Fig. 4(a), one observes that the Dirac cone at the Fermi level is contributed predominantly by Mo $d_{xz,yz}$ orbitals. The $d_{xz,yz}$ orbitals are degenerate at Γ point which possesses D_{4h} symmetry, and form a bonding π state and an antibonding π^* state below and above the Fermi level, respectively. Along the Γ-M path, the degenerate $d_{xz,yz}$ bands split into two branches since the symmetry is reduced to C_{2v}. The lower π band and the higher π^* band cross each other to form the Dirac cone since they belong to different representations (A_2 and B_2, respectively), which prevents hybridization between them. Therefore, the band crossing in the spin-up channel is unavoidable. On the contrary, the hybridization between the Mo $d_{x^2-y^2}$ and S p orbitals opens a gap in the spin-down channel, as shown in Fig. 4(b).

Before we discuss the SOC effect on the band structure and the band topology of the 1P-MoS_2 monolayer on the CuI(001) substrate, the band structure with SOC and the QAH state of the pristine 1P-MoS_2 are demonstrated, as shown in Fig. S5 [43]. The SOC effect lowers the symmetry along the Γ-M path from C_{2v} point group to C_s magnetic double point group. Under C_s symmetry, the two bands have the same representation of Γ_3. Therefore, the hybridization between them opens

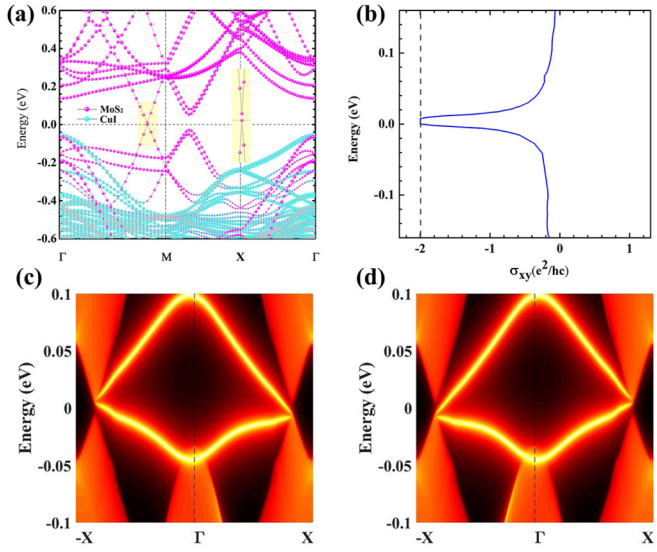

FIG. 5. (a) Band structure of the 1P-MoS_2/CuI(001) surface with SOC considered, where magenta and cyan balls represent the contributions of 1P-MoS_2 and CuI(001), respectively, while the size of balls is in proportion to the contribution. (b) Anomalous Hall conductivity as a function of the Fermi level for the 1P-MoS_2 monolayer. (c–d) Edge densities of states of semi-infinite nanoribbon constructed based on isolated 1P-MoS_2 for the left and right edges, respectively.

a gap in the 1P-MoS_2 monolayer when the SOC interaction is considered. Here we observe that, with SOC included, the splitting of linear crossing bands introduces a gap of 3 meV into the 1P-MoS_2/CuI(001) system. Interestingly, as indicated in Fig. 5(a), the energy bands in the vicinity of the Fermi level are dominantly contributed by 1P-MoS_2, confirming that the interaction between 1P-MoS_2 and CuI(001) substrate is rather weak. We therefore have reasons to isolate the 1P-MoS_2 sheet from the combined system, to examine its band topology without carrying out any further structural optimization.

In order to calculate the anomalous Hall conductivity(AHC), we follow the Berry phase formalism [52], within which AHC is determined by a sum of Berry curvature $\Omega^z(\mathbf{k})$ over all k points within the Brillouin zone (BZ) for all occupied bands,

$$\sigma_{xy} = -\frac{e^2}{h}\int_{\mathrm{BZ}} \frac{d^3k}{(2\pi)^3}\Omega^z(\mathbf{k}) \tag{3}$$

$$\Omega^z(\mathbf{k}) = -\sum_{m\neq n} \frac{2\mathrm{Im}\langle\psi_{nk}|\hat{v}_x|\psi_{mk}\rangle\langle\psi_{mk}|\hat{v}_y|\psi_{nk}\rangle}{(\omega_m-\omega_n)^2}, \tag{4}$$

where $\hat{v}_x$ and $\hat{v}_y$ are velocity operators. We then employ the efficient Wannier interpolation method on the basis of maximally localized Wannier functions (MLWFs) as implemented in the WANNIER90 package [53–55] to meet the requirement of a large number of k point sampling for an accurate evaluation of the AHC. Twenty MLWFs of Mo d orbitals, which have a dominant contribution to the energy bands near the Fermi level, are constructed to fit the *ab initio* relativistic band structure. The AHC is then calculated with a very dense k-point mesh of 150 × 150 × 1. As indicated in Fig. 5(b), the quantized AHC of $-2e^2/hc$ persists in the 1P-MoS_2 overlayer, and yields a Chern number of $|C| = 2$. To further verify

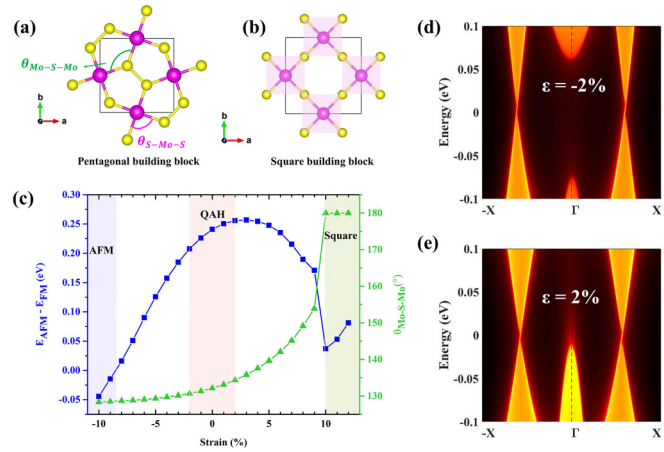

FIG. 6. (a–b) Structural motifs under strains. (c)The variations of exchange energy and band gap as a function of strains. (d–e) The edge densities of states for the stretched 1P-MoS_2 at $\varepsilon = -2\%$ and $\varepsilon = 2\%$, respectively. Only the right-hand edges are shown here.

the robustness of the edge state, we employ the MLWFs to construct the edge Green's function [56] for a semi-infinite nanoribbon with a width of 18.12 nm based on the isolated 1P-MoS_2 monolayer via the WANNIERTOOLS code [57]. The calculated edge density of states for the left and right edges are shown in Figs. 5(c) and 5(d), respectively. Apparently, each edge has two topological nontrivial edge states with identical chirality connecting the valence band maximum and the conduction band minimum. These results prove a robust QAH effect existing in the 1P-Mos2/CuI(001) heterostructure. Consequently, a quantum transport device could be designed on the basis of the 1P-MoS_2/CuI(001) heterostructure, as illustrated in Fig. 2(b).

E. Strain effect on the QAH state

In order to check the robustness of the QAH state against the lattice variation, we investigate the strain effect on the structural, magnetic, and electronic properties of the 1P-MoS_2 monolayer. When subjected to a biaxial strain, the S-Mo-S bond angle (θ_{S-Mo-S}) remains 90°, while the Mo-S-Mo bond angle ($\theta_{Mo-S-Mo}$) increases as the lattice expands. The $\theta_{Mo-S-Mo}$ abruptly becomes 180° at strain ε=10%, leading to the transformation of building blocks from planar pentagons to planar squares, see Figs. 6(a)–6(c). Besides, our results reveal that when the applied compressive strain is larger than 8%($\varepsilon < -8\%$), the AFM state turns out to be the ground state. Within the strain range from - 8% to 2%, the exchange coupling between Mo atoms increases monotonically with the expanding of lattice and reaches the largest value of 31.96 meV at ε=2%. This result indicates a possible increase of T_c for 1P-MoS_2 under moderate tensile strain. The band structure calculations reveal that, within the strain range of −2% to 2%, the Fermi level still resides in the SOC induced band gap. Consequently, the QAH state is unaltered within this strain range, see Figs. 6(d) and 6(e) for the preserved edge states of the 1P-MoS_2 monolayer with −2% and 2% strain, respectively. However, there is a lack of a global band gap when the applied strain is out of this range. These results

may shed some light on determining an appropriate substrate apart from CuI(001) for epitaxial growth of 1P-MoS_2 without disturbing its topological nontrivial state.

IV. CONCLUSION

In summary, we have predicted that the CuI(001) surface, which perfectly matches the 1P-MoS_2 monolayer, constitutes a good substrate candidate for 1P-MoS_2. First of all, the CuI(001) surface plays an important role in stabilizing the 1P-MoS_2 monolayer by providing a tensile strain that is required to beat the buckled rivals. Besides, the 1P-MoS_2/CuI(001) system is thermodynamically stable at room temperature. More importantly, the intrinsic ferromagnetism and the QAH state of 1P-MoS_2 are well preserved in the 1P-MoS_2/CuI(001) system. We also found that the QAH state of 1P-MoS_2 is robust within the strain range from -2% to 2%, indicating that alternative substrates which have a lattice mismatch with 1P-MoS_2 within this range can also be used to support the 1P-MoS_2 monolayer without disturbing its nontrivial band topology. These results broaden the possibility of realizing QAH effects of the 1P-MoS_2 monolayer in experiments.

ACKNOWLEDGMENTS

This work is supported by the National Natural Science Foundation of China (Grants No. 11574257 and No. 11874307), the National Key Research and Development Program of China (Grant No. 2016YFB0901502), and the Fundamental Research Funds for the Central Universities (Grants No. 20720180020 and No. 20720190050).

[1] C. L. Kane and E. J. Mele, Phys. Rev. Lett. **95**, 226801 (2005).
[2] B. A. Bernevig, T. L. Hughes, and S.-C. Zhang, Science **314**, 1757 (2006).
[3] M. König, S. Wiedmann, C. Brüne, A. Roth, H. Buhmann, L. W. Molenkamp, X.-L. Qi, and S.-C. Zhang, Science **318**, 766 (2007).
[4] X.-L. Qi and S.-C. Zhang, Phys. Today **63**(1), 33 (2010).
[5] D. J. Thouless, *Topological Quantum Numbers in Nonrelativistic Physics* (World Scientific, Singapore 1998).
[6] B. I. Halperin, Phys. Rev. B **25**, 2185 (1982).
[7] J. Maciejko, T. L. Hughes, and S.-C. Zhang, Annu. Rev. Condens. Matter Phys. **2**, 31 (2011).
[8] R. Yu, W. Zhang, H.-J. Zhang, S.-C. Zhang, X. Dai, and Z. Fang, Science **329**, 61 (2010).
[9] C.-Z. Chang, J. Zhang, X. Feng, J. Shen, Z. Zhang, M. Guo, K. Li, Y. Ou, P. Wei, L.-L. Wang *et al.*, Science **340**, 167 (2013).
[10] X. Kou, S.-T. Guo, Y. Fan, L. Pan, M. Lang, Y. Jiang, Q. Shao, T. Nie, K. Murata, J. Tang *et al.*, Phys. Rev. Lett. **113**, 137201 (2014).
[11] T. P. Kaloni, N. Singh, and U. Schwingenschlögl, Phys. Rev. B **89**, 035409 (2014).
[12] H. Zhang, C. Lazo, S. Blügel, S. Heinze, and Y. Mokrousov, Phys. Rev. Lett. **108**, 056802 (2012).
[13] B. Huang, G. Clark, E. Navarro-Moratalla, D. R. Klein, R. Cheng, K. L. Seyler, D. Zhong, E. Schmidgall, M. A. McGuire, D. H. Cobden *et al.*, Nature **546**, 270 (2017).
[14] C. Gong, L. Li, Z. Li, H. Ji, A. Stern, Y. Xia, T. Cao, W. Bao, C. Wang, Y. Wang *et al.*, Nature **546**, 265 (2017).
[15] Y.-P. Wang, S.-S. Li, C.-W. Zhang, S.-F. Zhang, W.-X. Ji, P. Li, and P.-J. Wang, J. Mater. Chem. C **6**, 10284 (2018).
[16] Z. F. Wang, Z. Liu, and F. Liu, Phys. Rev. Lett. **110**, 196801 (2013).
[17] X. Ni, W. Jiang, H. Huang, K.-H. Jin, and F. Liu, Nanoscale **10**, 11901 (2018).
[18] X. Kong, L. Li, O. Leenaerts, W. Wang, X.-J. Liu, and F. M. Peeters, Nanoscale **10**, 8153 (2018).
[19] S.-J. Zhang, C.-W. Zhang, S.-F. Zhang, W.-X. Ji, P. Li, P.-J. Wang, S.-S. Li, and S.-S. Yan, Phys. Rev. B **96**, 205433 (2017).
[20] P. Zhou, C. Sun, and L. Sun, Nano Lett. **16**, 6325 (2016).
[21] H. Liu, J.-T. Sun, M. Liu, and S. Meng, J. Phys. Chem. Lett. **9**, 6709 (2018).
[22] X.-L. Sheng and B. K. Nikolić, Phys. Rev. B **95**, 201402(R) (2017).
[23] S. Zhang, J. Zhou, Q. Wang, X. Chen, Y. Kawazoe, and P. Jena, Proc. Natl. Acad. Sci. U.S.A. **112**, 2372 (2015).
[24] Y. Wang, Y. Li, and Z. Chen, J. Mater. Chem. C **3**, 9603 (2015).
[25] A. D. Oyedele, S. Yang, L. Liang, A. A. Puretzky, K. Wang, J. Zhang, P. Yu, P. R. Pudasaini, A. W. Ghosh, Z. Liu *et al.*, J. Am. Chem. Soc. **139**, 14090 (2017).
[26] L. Liu and H. L. Zhuang, Phys. Rev. Mater. **2**, 114003 (2018).
[27] Z. Liu, H. Wang, J. Sun, R. Sun, Z. Wang, and J. Yang, Nanoscale **10**, 16169 (2018).
[28] H. Yuan, Z. Li, and J. Yang, J. Mater. Chem. C **6**, 9055 (2018).
[29] K. Zhao, X. Li, S. Wang, and Q. Wang, Phys. Chem. Chem. Phys. **21**, 246 (2019).
[30] Y. Ma, L. Kou, X. Li, Y. Dai, and T. Heine, NPG Asia Mater. **8**, e264 (2016).
[31] H. Zhang, Y.-M. Dai, and L.-M. Liu, Comput. Mater. Sci. **101**, 255 (2015).
[32] L. Liu, I. Kankam, and H. L. Zhuang, Phys. Rev. B **98**, 205425 (2018).
[33] H. Wang, F. Fan, T. Zeng, and G. Chen, J. Magn. Magn. Mater. **475**, 83 (2019).
[34] X. Li, S. Meng, and J.-T. Sun, Phys. Rev. B **101**, 144409 (2020).
[35] G. Kresse and D. Joubert, Phys. Rev. B **59**, 1758 (1999).
[36] G. Kresse and J. Furthmüller, Comput. Mater. Sci. **6**, 15 (1996).
[37] G. Kresse and J. Furthmüller, Phys. Rev. B **54**, 11169 (1996).
[38] J. P. Perdew, K. Burke, and M. Ernzerhof, Phys. Rev. Lett. **77**, 3865 (1996).
[39] H. J. Monkhorst and J. D. Pack, Phys. Rev. B **13**, 5188 (1976).
[40] A. Togo, F. Oba, and I. Tanaka, Phys. Rev. B **78**, 134106 (2008).
[41] S. Grimme, J. Comput. Chem. **27**, 1787 (2006).
[42] G. J. Martyna, M. L. Klein, and M. Tuckerman, J. Chem. Phys. **97**, 2635 (1992).
[43] See Supplemental Material at http://link.aps.org/supplemental/10.1103/PhysRevB.103.115131 for supplementary notes, Figs. S1-S5, and Table S1, which include Refs. [23,44–47].

[44] F. Liu, P. Ming, and J. Li, Phys. Rev. B **76**, 064120 (2007).
[45] J. F. Nye, *Physical Properties of Crystals: Their Representation by Tensors and Matrices* (Oxford University Press, Oxford, 1985).
[46] M. Born and K. Huang, *Dynamical Theory of Crystal Lattices* (Clarendon Press, Oxford, 1954).
[47] R. C. Cooper, C. Lee, C. A. Marianetti, X. Wei, J. Hone, and J. W. Kysar, Phys. Rev. B **87**, 035423 (2013).
[48] X. Ming, C. Autieri, K. Yamauchi, and S. Picozzi, Phys. Rev. B **96**, 205158 (2017).
[49] N. D. Mermin and H. Wagner, Phys. Rev. Lett. **17**, 1133 (1966).
[50] P. Giannozzi, S. Baroni, N. Bonini, M. Calandra, R. Car, C. Cavazzoni, D. Ceresoli, G. L. Chiarotti, M. Cococcioni, I. Dabo *et al.*, J. Phys.: Condens. Matter **21**, 395502 (2009).
[51] R. F. Evans, W. J. Fan, P. Chureemart, T. A. Ostler, M. O. Ellis, and R. W. Chantrell, J. Phys.: Condens. Matter **26**, 103202 (2014).
[52] Y. Suzuki, T. Katayama, S. Yoshida, K. Tanaka, and K. Sato, Phys. Rev. Lett. **68**, 3355 (1992).
[53] N. Marzari and D. Vanderbilt, Phys. Rev. B **56**, 12847 (1997).
[54] I. Souza, N. Marzari, and D. Vanderbilt, Phys. Rev. B **65**, 035109 (2001).
[55] A. A. Mostofi, J. R. Yates, G. Pizzi, Y.-S. Lee, I. Souza, D. Vanderbilt, and N. Marzari, Comput. Phys. Commun. **185**, 2309 (2014).
[56] M. L. Sancho, J. L. Sancho, J. L. Sancho, and J. Rubio, J. Phys. F: Met. Phys. **15**, 851 (1985).
[57] Q. Wu, S. Zhang, H.-F. Song, M. Troyer, and A. A. Soluyanov, Comput. Phys. Commun. **224**, 405 (2018).